Lab on a Chip RSCPublishing

ARTICLE

Magnetic Nanocomposite for Biomimetic Flow Sensing

Cite this: DOI: 10.1039/x0xx00000x

A. Alfadhel,[a] B. Li,[a] A. Zaher,[a] O. Yassine,[a] and J. Kosel[a]

Received 18th July 2014,
Accepted 18th August 2014

DOI: 10.1039/x0xx00000x

www.rsc.org/

A magnetic nanocomposite has been implemented as artificial hair on a giant magneto-impedance (GMI) thin film sensor for flow sensing. The 500 µm long and 100 µm in diameter pillars are composed of iron nanowires incorporated in polydimethylsiloxane (PDMS). The nanowires' length and diameter are 6 µm and 35 nm, respectively. Upon fluid flow, the pillars are deflected, causing a change of the magnetic field at the GMI element and a corresponding impedance change. The permanent magnetic behavior of the nanowires in combination with the GMI sensor and the high elasticity of the PDMS pillars results in a high performance flow sensor with low power consumption and potential for remote detection. No additional magnetic field is required to magnetize the nanowires or bias the sensor, which simplifies miniaturization and integration in microsystems. At a power consumption of 31.6 µW, air flow rates up to 190 mm/s can be detected with a sensitivity of 24 mΩ/(mm/s) and a resolution of 0.56 mm/s while the range for water flow is up to 7.8 mm/s with a sensitivity of 0.9 Ω/(mm/s) and a resolution of 15 µm/s. When the power consumption is reduced to as little as 80 nW a high resolution of 32 µm/s is still maintained.

Introduction

Cilia are micro-scale, hair-like structures that exist in nature and extend from the organism's cells. Taking fish as an example, the hair cells assist in performing a variety of functions such as preying or avoiding danger. When the cilia are exposed to a change in the fluid flow, they bend and transmit a signal to the organism. This signal is then translated into a specific function.

Recently, artificial cilia have been developed that could be used for various applications such as cell mechanics study,[1,2] microfluidic propulsion,[3,4] and flow sensing.[5] For the hair flow sensors, different techniques have been utilized to detect cilia bending, due to flow such as thermal, piezoresistive, piezoelectric and magnetic.[5]

A piezoresistive hair flow sensor realized by Chen et al. consists of a 600 µm by 80 µm vertical SU-8 hair-like structure fabricated by photolithography and a silicon resistor. The sensor was able to detect constant air flow between 0 to 20 m/s with a resolution of 100 mm/s and water flow from 0 to 0.4 m/s with a resolution of 5 mm/s. The sensor was also able to detect alternating flow velocity amplitudes down to the order of 0.7 mm/s in water at a frequency of 50 Hz.[6]

Flow sensors based on a vertical cilium and a strain gauge were developed by Liu et al. The study included two prototypes: silicon-based and polymer-based cilia. The silicon-based sensor was mounted on a glass plate and placed in a water tunnel with laminar flow. For water flows with velocities from 0 to 1 m/s, a sensitivity of 0.5 mm/s was reported. The response of the polymer-based sensor increases exponentially within the tested range, when applying air flow with velocities ranging from 0 to 30 m/s. Chang concluded that silicon-based flow sensors showed higher sensitivity, whereas polymer-based sensors were more robust.[7]

Hein et al. proposed an inorganic nanocilia sensor based on magnetic nanowires (NWs) that utilizes the magnetic stray field of cobalt NWs for a biomimetic sensing approach. The NWs are mounted on a giant-magneto-resistive sensor to detect their motion. The sensor has two possible applications: flow sensing and vibration sensing. Water flows were detected from 3.3 m/s to 40 m/s with a sensitivity of 0.55 µV/m/s and a signal to noise ratio of 44, and vibrations in the low earthquake-like frequency range of 1–5 Hz.[8] The stiffness of the bare magnetic NWs prevents the measurement of low flow velocities. Nanocilia made of metals like Co have high possibility of corrosion, limiting their use for applications in, e.g., microfluidic devices. Magnetic polymer cilia have also been realized using superparamagnetic nanoparticles embedded in thin polymer films for various applications.[3,9] This approach requires the application of rather large magnetic fields. For instance, Khaderi et al. applied a rotational magnetic field of 115 mT in amplitude and Digabel et al. used 23×10^3 T.m^{-1} magnetic field gradient to actuate the cilia. A favorable property of magnetic cilia is the absence of an electric contact and the possibility of remote detection or actuation.[10]

Recently, there has been a great interest in developing sensors with low power consumption. However, reducing the power consumption usually leads to a reduction in the resolution. For example, a low power thermal flow sensor developed by Cubukcua et al. shows a resolution below 10 mm/s at 177 µW.[11] High resolution thermal flow sensors have a power consumption of more than 1 mW.[12] In this regard, hair flow sensors are attractive options and have been shown to operate at a power consumption as low as 140 µW providing a resolution of 0.9 m/s.[8]

In this work, we describe a magnetic polymer hair flow sensor that provides both a high resolution and a very low power consumption. The sensor is composed of cylindrical polydimethylsiloxane (PDMS) pillars containing iron NWs and implemented on a giant magnetoimpedance (GMI) thin film sensor, which was chosen for its simple and cheap fabrication,[13] high sensitivity[13,14] and potential for wireless operation.[15] The high elasticity of the magnetic-PDMS composite[16] enables the detection of extremely low flow velocities. These advantages, together with the good resistance to corrosion, make the proposed hair flow sensor suitable for many applications.

Methods

1. Concept

The flow sensor is composed of eight PDMS pillars that are 500 µm long and 100 µm in diameter, and which have iron NWs with 6 µm in length and 35 nm in diameter incorporated. The magnetic nanocomposite pillars are fabricated on top of a GMI sensor (Fig. 1).

[a]Computer, Electrical and Mathematical Sciences and Engineering Division (CEMSE), King Abdullah University of Science and Technology (KAUST), Thuwal 23955, Saudi Arabia. Email: ahmed.fadhel@kaust.edu.sa

† Electronic Supplementary Information (ESI) available: [details of any supplementary information available should be included here]. See DOI: 10.1039/b000000x/

The operating principle of the flow sensor is based on detecting the change of the magnetic field, created by the permanent magnetic NWs, of the magnetic-PDMS pillars, when deflected by a fluid flow. A multi-layer GMI sensor, which offers a good compromise between sensitivity[17] and fabrication complexity, is utilized to measure the change of the magnetic field. At small bias fields and at high operating frequencies, the impedance of GMI sensors is sensitive to external magnetic fields, due to the strong dependence of the skin effect on the magnetic permeability. A distinct advantage of the this flow sensor is the permanent magnetic behavior of the iron NWs in the nanocomposite pillars, remedying the need for an external magnetic field to magnetize the pillars or bias the GMI sensor. At resting position, the stray field of the pillars affects the GMI sensor with an average magnetic field value $H(0)$ that biases the sensor and changes its initial impedance. In the presence of a fluid flow, the pillars bend in the flow direction. This bending results in a change of the stray field of the pillars with an average magnetic field value $H(\delta)$ affecting the GMI sensor, and hence changing its impedance.

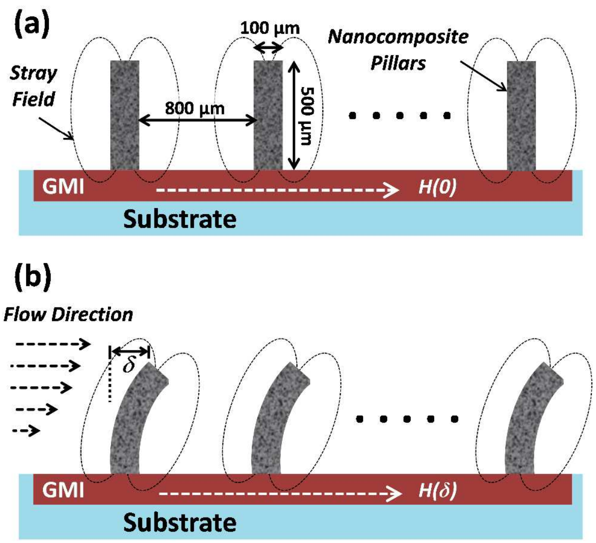

Fig. 1: Illustration of the flow sensor operation principle. (a) A GMI sensor is used to detect the stray field of the magnetic nanocomposite pillars, which is, on average, $H(0)$ without fluid flow. (b) Fluid flow causes the pillars to bend (δ is the tip deflection), changing the average field to $H(\delta)$.

The flow signal is obtained as the impedance change ΔZ, which is the difference between the GMI sensor's impedance Z_δ, when a flow is applied and the pillars' tips are deflected by δ, and the initial impedance Z_0, when no flow is applied and $\delta = 0$. The impedance can be calculated from the average magnetic field value at the GMI sensor and the sensitivity of the GMI sensor S_{GMI}, which is assumed to be constant about the operation point. The sensitivity S of the flow sensor is the impedance change over the average flow velocity $v_{avg}(\delta)$:

$$S = \frac{\Delta Z}{v_{avg}(\delta)} = \frac{Z_\delta - Z_0}{v_{avg}(\delta)} = \frac{S_{GMI}[H(\delta) - H(0)]}{v_{avg}(\delta)}. \tag{1}$$

Using S together with the maximum impedance fluctuation Z_f (noise), the resolution is:

$$R = Z_f / S. \tag{2}$$

The velocity inside the fluidic channel for a laminar flow is not constant but changes across the cross section area of the channel. The velocity is highest along the center of the channel and it is reducing toward the channel walls. The average flow velocity v_{avg} is estimated to be one half of the maximum flow velocity.[18]

Using the displacement-force relationship of an elastic cylindrical beam, the value of δ can be expressed for uniformly distributed forces F along the length of the pillar as:[19]

$$\delta = \frac{64}{3} F \frac{l^3}{\pi E D^4} = \frac{64}{3}\left(\frac{1}{2}\rho v_{avg}(\delta)^2 C_D A(\delta)\right)\frac{l^3}{\pi E D^4}, \tag{3}$$

where l, E, and D are the length, the Young's modulus and the diameter of the pillars, respectively. The force is proportional to the fluid density ρ, drag coefficient C_D and the area of the pillars that is facing the flow $A(\delta)$, which is a function of δ, since the effective area is reducing as the pillars bend. C_D is computed by:[20]

$$C_D = 0.8 + \frac{13.6}{Re} = 0.8 + \left(\frac{13.6\mu}{\rho v_{avg}(\delta) D_h}\right), \tag{4}$$

where Re is the Reynolds number, D_h is the hydraulic diameter and μ is the fluid dynamic viscosity.

Besides its advantages like chemical resistance, PDMS is specifically chosen for its low Young's modulus value, making the pillars highly elastic and easy to bend at small flow velocities.

2. Fabrication

The 8 mm long and 400 µm wide multi-layer GMI sensor is composed of a 200 nm thick Cu layer sandwiched by two 100 nm thick $Ni_{80}Fe_{20}$ layers. The materials are deposited onto a glass substrate by e-beam evaporation with a constant magnetic field of 100 Oe applied in the transverse direction to induce a uniaxial magnetic anisotropy, creating a magnetically sensitive axis in the longitudinal direction. The sensor is patterned by a lift-off process (Fig. 2a).

Iron NWs are fabricated by electrodeposition in nanoporous aluminum oxide, prepared by a two-step anodization process using oxalic acid on an aluminum substrate.[21] Iron is chosen for its high magnetization at remanence and high coercivity, creating a large stray field and making the pillars hard to demagnetize. Moreover, iron NWs have shown to be biocompatible,[22] and can be efficiently fabricated with this process with a high control of the properties.

The nanocomposite pillars are fabricated using a 500 µm thick poly(methylmethcrylate) (PMMA) master mold into which an array of eight holes, separated by 800 µm and each having 100 µm in diameter, is patterned with a CO_2 laser cutter (Universal PLS6.75). The nanocomposite is prepared by mixing iron NWs in PDMS (Sylgard 184 Silicone Elastomer, Dow Corning Corporation) that is used as the polymeric matrix with 18% NWs to PDMS volume ratio. This ratio is sufficient to provide the biasing field for the GMI sensor; yet, it does not adversely affect the polymerization process of the PDMS or the elasticity of the pillars. The composite is casted onto the surface of the substrate and the master mold is mounted on top of it such that the pillars are aligned along the GMI sensor (Fig. 2b, c). This structure is then placed in a desiccator for 30 minutes to remove any trapped air bubbles and assist in filling the pores. Next, the composite is cured at 90 degrees Celsius for 1 hour, forming the pillars on top of the GMI sensor's surface. After releasing the cured pillars, they are fully magnetized by applying a magnetic field of 10 kOe.

The flow sensor is tested inside a fluidic channel, which is 1 mm high, 10 mm wide and 15 mm long and has an inlet and an outlet (Fig. 2d). The channel is fabricated with the laser cutter using three layers of PMMA substrates bonded by applying chloroform at the bonding joints and pressing the substrates by hand. The channel is then bonded to the sensor's substrate using instant room temperature curing adhesive. The channel provides a small value of Re to avoid turbulence and achieve laminar flow.

The fabricated nanocomposite pillars on the GMI sensor are shown in Fig. 3. The bottom diameter of the pillars is slightly wider than the top diameter, which is a result of patterning the mold with the laser beam.

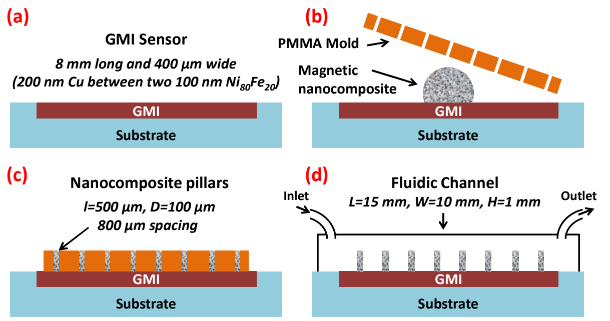

Fig. 2: Illustration of the flow sensor fabrication process. (a) A GMI sensor fabricated on a glass substrate. (b) A nanocomposite consisting of PDMS and magnetic NWs is placed on the substrate, and (c) a PMMA mold is mounted onto the composite. Then, the composite is cured at 90 °C for 1 hour. (d) The PMMA mold is removed, and the sensor is integrated in a PMMA fluidic channel.

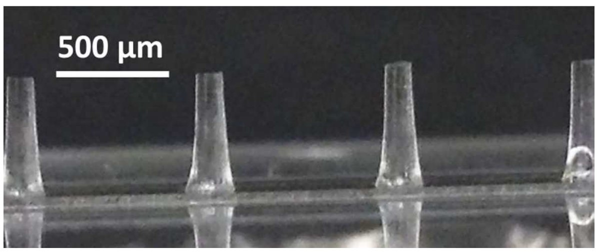

Fig. 3: Optical image of the fabricated nanocomposite pillars with 500 µm in length and 100 µm in diameter.

3. Characterization

Since a high elasticity of the nanocomposite pillars is crucial for a high sensitivity, the influence of the NWs on the Young's modulus is evaluated by applying a constant force of 0.5 N to a 2 cm long, 1 cm wide and 500 µm thick PDMS sample with 18% NWs. The nanocomposite has a Young's modulus of 270 kPa, which is only a slightly higher value than the 255 kPa found for a pure PDMS sample prepared with the same conditions. Hence, the advantage of the high elasticity of the PDMS is maintained.

In order to test the magnetic properties, the magnetization curves along the length of the pillars and along the perpendicular direction are obtained using a vibrating sample magnetometer. As shown in Fig. 4, the nanocomposite pillars have a remanence magnetization of 2.1 memu and a remanence to saturation magnetization ratio of 0.7 with a coercivity of 1520 Oe. The similarity of the magnetization curves in the vertical and horizontal directions indicates that the NWs are not fully aligned in a specific direction in the composite, with the vertical direction being slightly preferred. Electron microscopy images show the distribution of the NWs inside the pillars (Fig. 5a) and are used to determine the length of the NWs (Fig. 5b). X-ray diffraction analysis reveals the NWs are polycrystalline iron with a thin shell of magnetite around the NWs (Fig. 6).

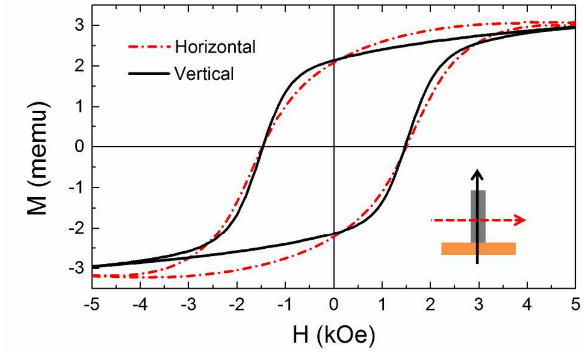

Fig. 4: The nanocomposite pillars' magnetization *M* as a function of the applied field *H* obtained with a vibrating sample magnetometer in the vertical and horizontal direction with respect to the pillars' axes.

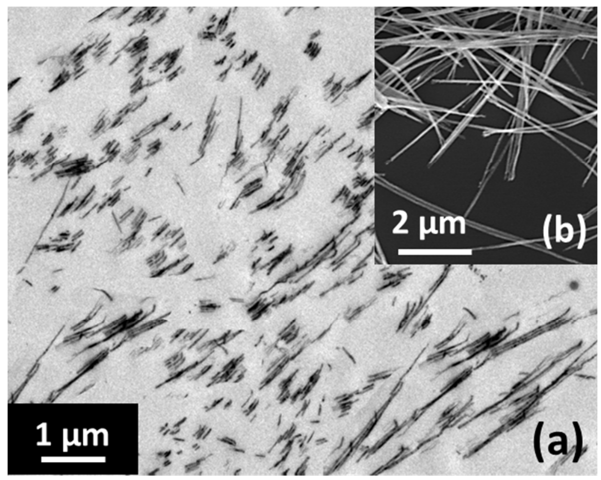

Fig. 5: (a) Transmission electron microscope cross section image of a nanocomposite pillar (b) Scanning electron microscope image of 6 µm long and 35 nm in diameter iron nanowires.

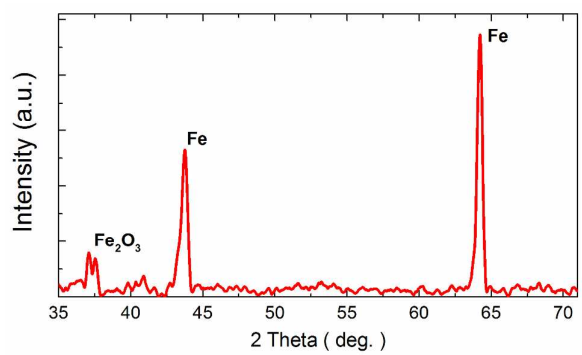

Fig. 6: X-ray diffraction results for iron nanowires.

Iron NWs can be easily oxidized when exposed to a humid environment reducing the magnetization of the NWs. In order to study this effect, the remanent magnetizations of a nanocomposite exposed to air and a nanocomposite kept in water are measured over a period of 60 days (Fig. 7). The magnetization drops over time with a reducing rate. The sample exposed to air keeps 81% of the initial magnetization while the sample kept in water keeps 76% of the initial magnetization. NWs inside the composite oxidize due to the fact that PDMS is permeable to water molecules. This explains the higher magnetization reduction rate for the sample kept in water. Fig. 7 also shows the remanent magnetizations of fully oxidized iron NWs that were oxidized by placing them in an oven for 24 hours at 150°C. These NWs oxidized forming magnetite as found by transmission electron microscopy. The magnetization of magnetite NWs is found to be 49% of that of iron NWs. This value is higher than the 30% reported in literature,[23] which we attribute to an oxide layer around the NWs at the beginning of the experiment. Comparing the oxidization rate of the nanocomposites to bare iron NWs (Fig. 7) shows that the latter oxidize with a much higher rate. After 10 days, the remanent magnetization of the bare wires in air drops to 85% of the initial magnetization compared to the 98% and 92.5% of nanocomposite exposed to air and water, respectively.

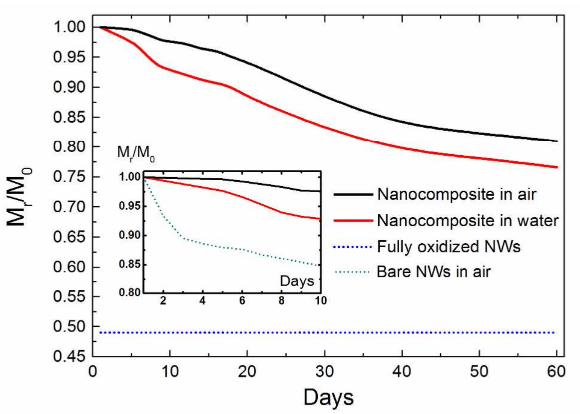

Fig. 7: Remanence magnetization M_r to initial remanence magnetization M_0 of nanocomposite pillars kept in air and water and of fully oxidized iron NWs. Inset: Comparison between nanocomposites and bare iron NWs.

Prior to testing the magnetic hair flow sensor, the GMI sensor is characterized in order to obtain the sensitivity S_{GMI}. Using a Helmholtz coil, a magnetic field from 0 Oe to 100 Oe with increments of 1 Oe is applied to the GMI sensor, and the impedance is obtained with an impedance analyzer (Agilent E4991A) at a current of 2 mA in amplitude and a frequency from 10 to 500 MHz (Fig. 8a). The GMI sensor response shows a peak at a field of 11 Oe corresponding to the anisotropy field of the $Ni_{80}Fe_{20}$ thin film. The response of the GMI sensor at 500 MHz and for fields applied in the longitudinal and transverse direction is shown in Fig. 8b. As can be seen, the GMI sensor is magnetically sensitive in the longitudinal direction while no significant impedance change is observed in the transverse direction. The GMI ratio, which is the maximum impedance change obtained with respect to the impedance at saturation field, is 20% and 1.3% in the longitudinal and transverse direction, respectively. This anisotropic magnetic property of the GMI sensor provides a good selectivity in terms of the direction of the magnetic signal that is being measured. The value of S_{GMI} is estimated through a linear fit of the GMI sensor's response between 0 Oe and 11 Oe, as shown in Fig. 8b, which includes the operating range, within which the magnetic fields are varying with the deflection. S_{GMI} increases with increasing frequency (Fig. 8c), therefore, 500 MHz is selected as the operating frequency, where S_{GMI} is 0.67 Ω/Oe.
The flow sensor is tested by applying air and water volumetric flow rates using a syringe pump through a channel inlet in both sensitive and non-sensitive directions of the GMI sensor. The average flow velocity is calculated by dividing the applied volumetric flow rate by the channel cross-section area of 10 mm^2. The impedance magnitude of the GMI sensor is measured with the impedance analyzer at a current of 2 mA in amplitude and 500 MHz in frequency. A set of 10 data points at every flow velocity value is recorded over a period of 30 seconds. The values for Z_δ and Z_f are obtained from the average value and the maximum deviation from the average value, respectively. The current dependence of the flow sensor is tested for current amplitudes between 0.1–10 mA, which are the limits of the impedance analyzer. The experimental setup is shown in Fig. 9.

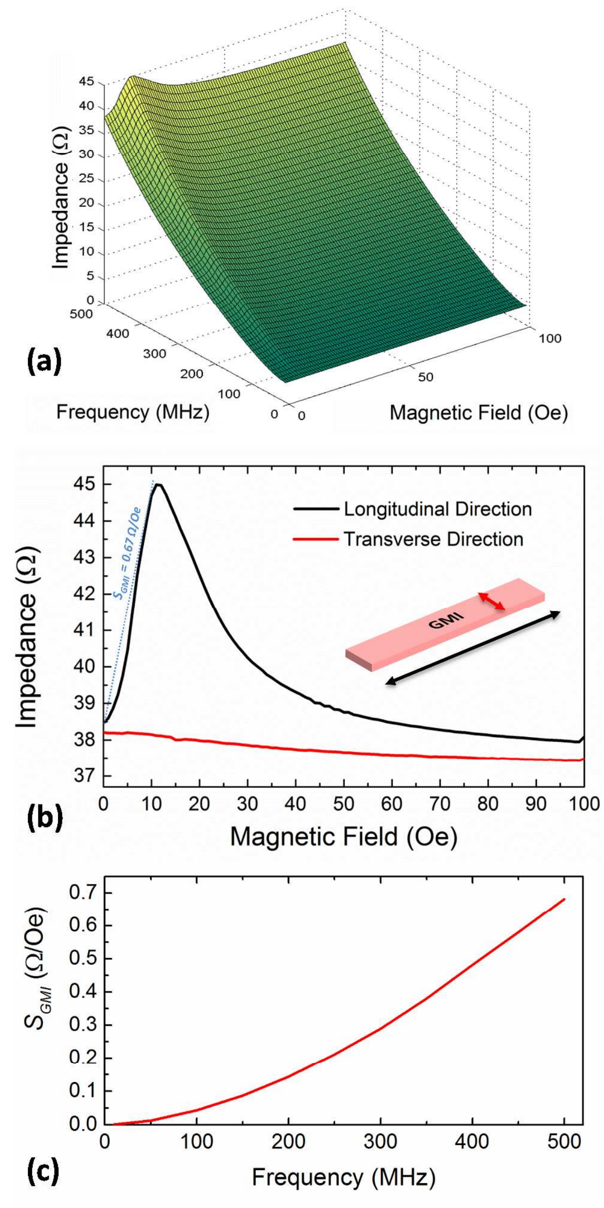

Fig. 8: (a) Impedance characterization of the GMI sensor as a function of the frequency and the magnetic field applied in the longitudinal direction. (b) Impedance response of the GMI sensor with external magnetic fields applied in the sensitive (longitudinal) and non-sensitive (transverse) directions at 500 MHz. The GMI sensor sensitivity S_{GMI} was determined by a linear fit. (c) S_{GMI} along the sensitive direction as a function of the frequency.

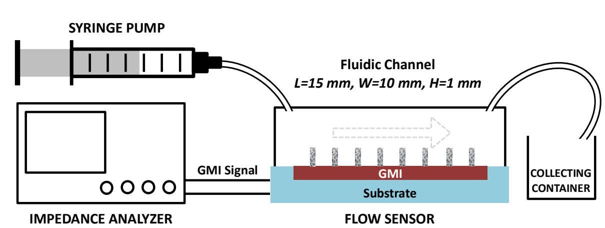

Fig. 9: Flow sensor experimental setup.

4. Computational Model

The response of the flow sensor is computed from eqn (1) and eqn (3) using a Young's modulus of 270 kPa, a remanence magnetization of 2.1 memu and S_{GMI} = 0.67 Ω/Oe. The eight pillars are modeled by finite element simulations using commercial software (COMSOL) as 3D cylindrical beams, in order to study the magnetic fields affecting the GMI sensor upon the deflection of the nanocomposite pillars. The magnetic NWs are accounted for by assigning flux density vectors to the pillars, which are calculated from the NWs' remanence value and the amount of NWs in the pillars. Fluid flow is simulated by rotating the pillars about the anchor point by the angle θ, which is related to the deflection by:

$$\delta = l\,.\sin(\theta). \tag{5}$$

This changes the effective area of the pillar that is facing the flow to:

$$A(\theta) = \frac{\pi D}{2} l\,.\cos(\theta)\,. \tag{6}$$

The average value of the magnetic field at the GMI sensor is:

$$H(\theta) = \frac{1}{n}\sum_{i=1}^{n}(H_x)_i, \tag{7}$$

where H_x is the component of the magnetic vector field along the GMI sensor's sensitive direction, i is the summation index and n is the number of magnetic vectors used in the averaging process. The average magnitude of the magnetic field is calculated as:

$$H_{mag}(\theta) = \frac{1}{n}\sum_{i=1}^{n}.\left(\sqrt{{H_x}^2}\right)_i. \tag{8}$$

When the pillars are straight, an average magnetic vector field of 0 Oe is obtained, due to the symmetry of the stray field. However, the magnitude of the magnetic field in this case is 3.2 Oe, which can be considered as the bias field of the GMI sensor. As the pillars deflect, the stray field at the GMI sensor increases on one side of the pillar and decreases on the other side, causing the average magnetic field value to increase. When the pillars are fully deflected, the magnetic field reaches an average value of 1.3 Oe.

$v_{avg}(\delta)$ is calculated by combining eqn (4) with eqn (3), where $A(\delta)$ can be derived from eqn (5) and eqn (6) as:

$$A(\delta) = \frac{\pi D}{2}\left(\frac{\delta}{\sin(\theta)}\right).\cos(\theta) = \frac{\pi D\delta}{2\tan(\theta)}\,. \tag{9}$$

The flow sensor's impedance change can now be calculated from eqn (1) by relating $H(\delta)$ to the corresponding $H(\theta)$ and using S_{GMI} from the experiment.

Results and Discussion

The results of the flow experiments are shown in (Fig. 10a) for air and (Fig. 10b) for water, respectively. The sensor is sensitive to average air flow velocities from 0 to 190 mm/s with maximum values of S = 24 mΩ/(mm/s) and R = 0.56 mm/s. In case of water, the sensor operates in the range from 0 to 7.8 mm/s with maximum values of S = 0.9 Ω/(mm/s) and R = 15 µm/s. The range of flow rates is lower for water than for air, due to the higher density of water, causing larger forces to be exerted on the pillars. In both cases the response is increasing in a relatively linear manner (±5%) between 0 and 0.6 mm/s for water flow and between 0 and 18 mm/s for air flow, with the slopes representing the maximum sensitivity. Another linear region (±3%) is observed for water flow between 1.9 and 7.8 mm/s with S = 13.5 mΩ/(mm/s), and between 40 and 190 mm/s with S = 0.7 mΩ/(mm/s) for air. Completely bending the pillars results in saturating the impedance change at 0.53 Ω and 0.54 Ω for air and water flows, respectively.

The orientation of the fluidic channel with respect to the GMI sensor's alignment is changed, in order to test the flow sensor along the non-sensitive direction. A smaller response of about 10% compared to the sensitive direction is obtained with the saturation values of 0.059 Ω for air and 0.061 Ω for water.

Fig. 10 also shows the theoretical response of the flow, which is in close agreement with the experimental results. A slightly higher saturation value of 5.7 Ω is obtained from the theoretical model. This is most likely due to the actual magnetization of the pillars being lower than expected, indicating a lower NW concentration than expected. Theoretical impedance values at the knee region, which corresponds to around 70 degrees pillar deflection, are higher than the experimental values, due to the assumption of rotation of straight pillars rather than their bending and neglecting the fact that the actual flow velocity inside the channel is reducing toward the channel walls.

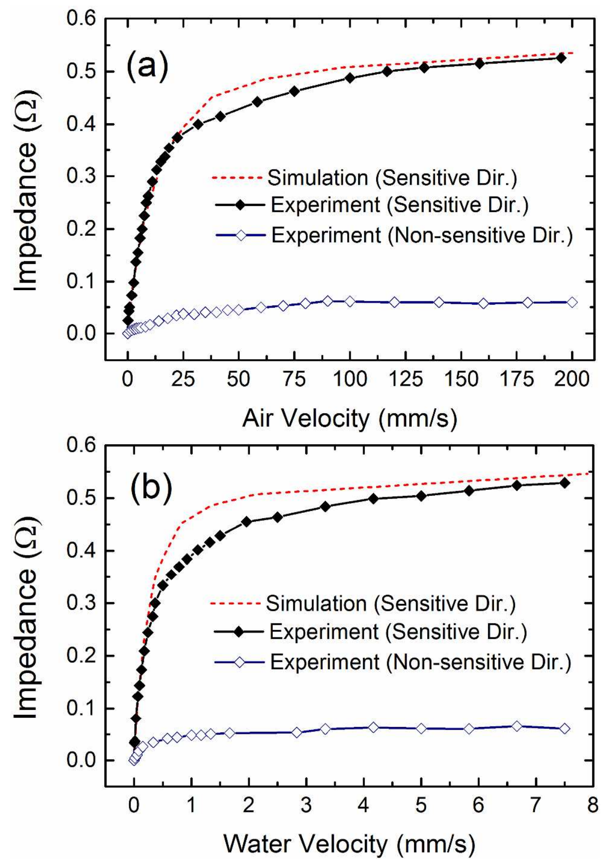

Fig. 10: Experimental and simulated impedance change of the flow sensor at different flow velocities along the GMI sensor's sensitive direction and non-sensitive direction for (a) air flow and (b) water flow.

The performance of the flow sensor can be modified easily by changing the mechanical parameters of the pillars. Changing the diameter of the pillars, for example, leads to a different operating range, resolution and sensitivity (Fig. 11). To demonstrate this point, a flow sensor is fabricated with 500 µm long and 250 µm in diameter nanocomposite pillars that have the same iron NWs volume as the 100 µm pillars. The modified sensor operates in the range from 0 to 12 mm/s with maximum values of S = 0.17 Ω/(mm/s) and R = 79 µm/s.

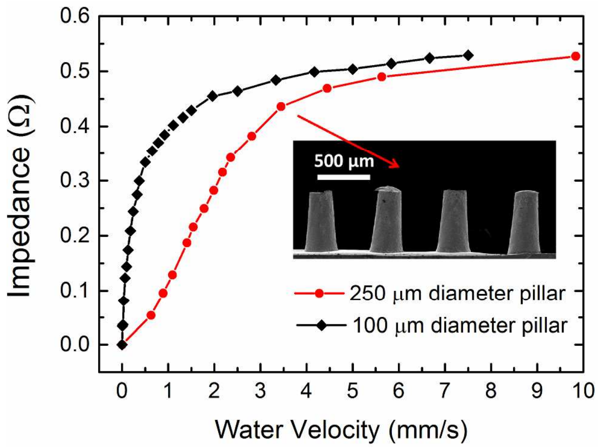

Fig. 11: Experimental impedance change of flow sensors with pillars of 100 µm and 250 µm in diameter and 500 µm in length at different flow velocities along the GMI sensor's sensitive direction for water flow. The fabricated pillars with 250 µm in diameter are shown in the inset.

The average power consumption of the flow sensor, when operated at 2 mA current amplitude, is 31.6 µW. The power consumption can be further reduced by operating the sensor at lower current amplitudes. The current dependence of the flow sensor is shown in Fig. 12. As can be seen, there is almost no influence of the current on the measured impedance value with slightly higher values obtained at low current amplitudes. The impedance of the GMI sensor at 2 mA driving current has fluctuations of Z_f = 0.0135 Ω, while Z_f = 0.0292 Ω and Z_f = 0.0096 Ω at 0.1 mA and 10 mA, respectively. This indicates that the signal stability can be enhanced by increasing the driving current, and hence increasing the resolution at the expense of power consumption. The operation at 10 mA leads to a slightly improved resolution of 10 µm/s at a power consumption of 790 µW. When operated at 0.1 mA, the power consumption can be reduced to as little as 80 nW, with the resolution still being 32 µm/s.

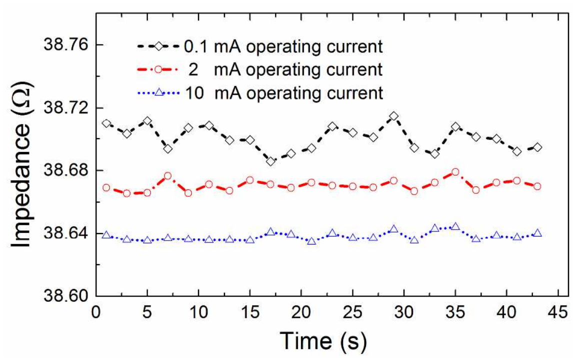

Fig. 12: Flow sensor impedance fluctuation over time for different current amplitudes.

Conclusion

Natural cilia are mimicked by nanocomposite pillars consisting of PDMS polymer with embedded iron nanowires. The pillars are permanent magnetic and have a high elasticity. They are integrated on a GMI thin film sensor to detect the change of the pillars' stray fields, resulting from bending them upon the application of fluid flow. The flow sensor can be used for both water and air flow measurement applications and has an operating range in case of air flow between 0 and 190 mm/s with a sensitivity up to 24 mΩ/(mm/s) and a resolution of 0.56 mm/s, and in case of water flow the operating range is between 0 and 7.8 mm/s with a sensitivity up to 0.9 Ω/(mm/s) and a resolution of 15 µm/s. The achieved resolution is high compared to previously reported flow sensors,[5-8,11,24] with a very low power consumption of 31.6 µW compared to reported thermal flow sensors with 177 µW[11] or hair flow sensors with 140 µW.[8] The power consumption can even be reduced to 80 nW, with only a small decrease of the resolution of water flow to 32 µm/s.

The magnetic NWs-based flow sensor proposed by Hein et al. offers the advantage of extremely small dimensions but suffers from the possibility of corrosion, and the high stiffness that prevents detection of low flow velocities. The developed magnetic nanocomposite flow sensor has a good corrosion resistance, is highly elastic, and uses a simple and cost-effective fabrication method compared with a conventional soft lithography process that demands templates prepared in specialized facilities with expensive consumables.

Eight pillars were used in the current sensor design, which were arranged in a manner allowing full deflection of each pillar without touching each other. This design provides an average signal over a length of 8 mm and can be readily adjusted to meet other requirements. This has been demonstrated by modifying the pillars' diameter from 100 µm to 250 µm, which increased the flow velocity range at the cost of sensitivity and resolution. The performance of the proposed hair flow sensor could be further improved by optimizing the sensitivity of the GMI sensor, which showed a rather small GMI ratio in our case. In general, other magnetic field sensors could also be used like contemporary magnetic tunnel junctions that might offer certain advantages over the GMI sensor. The advantage of the GMI sensor is its simple fabrication, robustness and the possibility to integrate the sensor with RF transducers for wireless operation, which could be useful for specific applications.

References

1 N. J. Sniadecki , A. Anguelouch , M. T. Yang , C. M. Lamb , Z. Liu, S. B. Kirschner, Y. Liu , D. H. Reich, and C. S. Chen, *PNAS*, 2007, **104**, 14553 .
2 A. Ghanbari, V. Nock, S. Johari, R. Blaikie, X. Chen, and W. Wang, *J. Micromech. Microeng.* 2012, **22**, 10.
3 S. N. Khaderi, C. B.Craus, J. Hussong, N. Schorr, J. Belardi, J. Westerweel, O. Prucker, J. Rühe, M. J. Toonder, and P. R. Onck, *Lab on a chip*, 2011, **11**, 2002.
4 F. Fahrni, M. J. Prins and L. IJzendoorn, *Lab on a chip*, 2009, **9**, 3413.
5 J. Tao and X. Yu, *Smart Materials and Structures*, 2012, **21**, 113001.
6 N. Chen, C. Tucker, J. Engel, C. Yang, S. Pandya, and C. Liu, *J. Microelectromech. Syst.*, 2007, **16**, 999.
7 C. Liu, *Bioinspiration and Biomimetic*, 2007, **2**, S162.
8 M. Hein , M. Maqableh , M. Delahunt , M. Tondra , A. Flatau , C. Shield , and B. Stadler, *IEEE Trans. on Magnetics*, 2013, **49**, 191.
9 J. Digabel, N. Biais, J. Fresnais, J. Berret, P. Hersen and B. Ladoux, *Lab on a chip*, 2011, **11**, 2630.
10 S Traxler, J Kosel, H Pfützner, E Kaniusas, L Mehnen, I Giouroudi, *Sensors and Actuators A: Physical*, 2008, **2**, 142.
11 A. Cubukcu, E. Zernickela, U. Buerklina, and G. Urbana, *Sensors and Actuators A*, 2010, **163**, 449.
12 J. Kuo, L. Yu, and E. Meng, *Micromachines*, 2012, **3**, 550.
13 M. Phan and H. Peng, *Progress in Materials Science*, 2008, **53**, 323.
14 L. V. Panina and K. Mohri, *Sens. Actuators A*, 2000, **81**, 71.
15 B. Li, P. Salem, I. Giouroudi, and J. Kosel, *Journal of Applied Physics*, 2012, **111**, 07E514.
16 K. Keshoju and L. Sun, *Journal of Applied Physics*, 2009, **105**, 023515.
17 B. Li, and J. Kosel, *Journal of Applied Physics*, 2011, **109**, 07E519.
18 Y. Cengel and J. Cimbala, in *Fluid Mechanics: Fundamentals and Applications*, McGraw-Hill, 2nd edn., 2010, vol. 1, ch. 8, pp. 321-342.
19 M. Yang, N. Sniadecki, and C. Chen, *Adv. Mater.*, 2007, **19**, 3119.
20 Y. Çengel and J. Cimbala, in *Fluid mechanics : fundamentals and applications*, ed. Suzanne Jeans, McGraw-Hill, USA, 1st edn.,2006, vol. 1, ch. 11, pp. 561-578.
21 K. Nielsch, F. Müller, A.P. Li, and U. Gösele, *Adv. Mater.*, 2000, **12**, 582.
22 M. Song, W. Song, H. Bi, J. Wang, W. Wu, J. Sun, and M. Yu, *Biomaterials*, 2010, **31**, 1509.
23 J. M. D. Coey, in *Magnetism and Magnetic Materials*, Cambridge University Press, UK, 2009, ch. 1, pp. 8.

24 A. Dagamseh, C.M. Bruinink, H. Droogendijk, R.J. Wiegerink, T.S. Lammerink, and G. Krijnen, Proceedings of the 9th IEEE Sensors Conference, Hawaii, USA, 2010.